



DEVELOPMENT AND VALIDATION OF REACTION WHEEL DISTURBANCE MODELS: EMPIRICAL MODEL

R. A. MASTERSON

*Space Systems Laboratory, Department of Aeronautics and Astronautics,
Massachusetts Institute of Technology, 77 Massachusetts Ave., Cambridge, MA 02139, U.S.A.
E-mail: beckym@alum.mit.edu*

D. W. MILLER

*Space Systems Laboratory, Department of Aeronautics and Astronautics,
Massachusetts Institute of Technology, 77 Massachusetts Ave., Cambridge, MA 02139, U.S.A.
E-mail: millerd@mit.edu*

AND

R. L. GROGAN

*Jet Propulsion Laboratory, California Institute of Technology, 4800 Oak Grove Drive, Pasadena,
CA 91109, U.S.A. E-mail: robert.l.grogan@jpl.nasa.gov*

(Received 19 June 2000, and in final form 28 June 2001)

Accurate disturbance models are necessary to predict the effects of vibrations on the performance of precision space-based telescopes, such as the Space Interferometry Mission (SIM). There are many possible disturbance sources on such spacecraft, but mechanical jitter from the reaction wheel assembly (RWA) is anticipated to be the largest. A method has been developed and implemented in the form of a MATLAB toolbox to extract parameters for an empirical disturbance model from RWA micro-vibration data. The disturbance model is based on one that was used to predict the vibration behaviour of the Hubble Space Telescope (HST) wheels and assumes that RWA disturbances consist of discrete harmonics of the wheel speed with amplitudes proportional to the wheel speed squared. The MATLAB toolbox allows the extension of this empirical disturbance model for application to any reaction wheel given steady state vibration data. The toolbox functions are useful for analyzing RWA vibration data, and the model provides a good estimate of the disturbances over most wheel speeds. However, it is shown that the disturbances are under-predicted by a model of this form over some wheel speed ranges. The poor correlation is due to the fact that the empirical model does not account for disturbance amplifications caused by interactions between the harmonics and the structural modes of the wheel. Experimental data from an ITHACO Space Systems E-type reaction wheel are used to illustrate the model development and validation process.

© 2002 Academic Press

1. INTRODUCTION

NASA's Origins program is a series of missions planned for launch in the early part of the 21st century that is designed to search for Earth-like planets capable of sustaining life and to answer questions regarding the origin of the universe. The first-generation missions include the Space Interferometry Mission (SIM), a space-based interferometer with astrometry and imaging capabilities [1], and the Next-Generation Space Telescope (NGST),

a near-infrared telescope.[†] These telescopes will employ new technologies to achieve large improvements in angular resolution and image quality and to meet the goals of high resolution and high-sensitivity imaging and astrometry [2]. The ability of these missions to accomplish their objectives will depend heavily on their structural dynamic behavior.

SIM and NGST pose challenging problems in the areas of structural dynamics and control since both instruments are large, flexible, deployed structures with precise stability requirements. The optical elements on SIM must meet positional tolerances of the order of 1 nm across the entire 10 m baseline of the structure to achieve astrometry requirements [3], and those on NGST must be aligned within a fraction of a wavelength to meet optimal observation requirements [4]. Disturbances from both the orbital environment and on-board mechanical systems and sensors are expected to impinge on the structure causing vibrations that can introduce jitter in the optical train and render the system unable to meet performance requirements. It is expected that the largest disturbances will be generated on-board and will be dominated by vibrations from the reaction wheel assembly (RWA) [3].

1.1. REACTION WHEEL ASSEMBLY

When maneuvering on orbit, spacecraft generally require an external force, or torque, that is sometimes provided by thrusters. As an alternative, RWA can counteract zero-mean torques on the spacecraft without the consumption of precious fuel and can store momentum induced by very low frequency or DC torques [5]. They are often used for both spacecraft attitude control [6] and large angle slewing maneuvers [7]. Other applications include vibration compensation and orientation control of solar arrays [8]. A typical RWA consists of a rotating flywheel suspended on ball bearings encased in a housing and driven by an internal brushless DC motor. Alternative RWA designs include the use of magnetic bearings to replace traditional ball bearings [9, 10].

During the manufacturing process, RWAs are balanced to minimize the vibrations that occur during operation. However, it has been found that the vibration forces and torques emitted by the RWA can still degrade the performance of precision instruments in space [7, 11–14]. In general, the RWA disturbance environment is driven by flywheel imbalance and bearing irregularities. Flywheel imbalance is the largest disturbance source in the RWA and induces a disturbance force and torque at the rate of rotation. There are two types of flywheel imbalances, static and dynamic. Static imbalance results from the offset of the center of mass of the wheel from its spin axis, and dynamic imbalance is caused by the misalignment of the wheel's principal axis and the axis of rotation [15]. Bearing disturbances, which are caused by irregularities in the balls, races, and/or cage [16], produce disturbances at both sub- and super-harmonics of the wheel's spin rate. In addition, lubricant dynamics can induce low-frequency disturbances and torque ripple and cogging in the brushless DC motor can generate very high-frequency disturbances [15].

1.2. DISTURBANCE MODELLING

Isolation systems have been used to reduce the effects of RWA disturbances on spacecraft requiring high levels of stability [7, 11, 13, 17]. Models of RWA-induced disturbances are generated for use in jitter analysis to predict the effects of the vibrations on the spacecraft

[†]see Origins website: <http://origins.jpl.nasa.gov>

and allow the development of suitable control and isolation techniques. One such disturbance model was developed to predict the effects of RWA-induced vibrations on the Hubble Space Telescope (HST) [14]. The model is based on induced vibration testing performed on the HST flight wheels and assumes that the disturbances are a series of harmonics at discrete frequencies with amplitudes proportional to the wheel speed squared. The model is fit to the vibration data and provides a prediction of the disturbances at a given wheel speed. However, during operation it is often necessary to run the RWAs at a range of speeds. Therefore, this discrete frequency model was later used to create a stochastic broad-band model that predicts the power spectral density (PSD) of RWA disturbances over a given range of wheel speeds [17]. The stochastic model assumes that wheel speed is a random variable with a given probability density function. Both the discrete frequency and stochastic models capture the disturbances of a single RWA. However, in application, multiple RWAs are used to provide multi-axis torques to the spacecraft and for redundancy. Therefore, a multiple-wheel model was developed which predicts the disturbance environment of multiple RWAs in a specified orientation based on a frequency domain disturbance model of a single wheel [4, 18]. In effect, the RWA disturbances from a frame attached to the RWA to the general spacecraft frame simplify the disturbance analysis.

The focus of this paper is the development of an empirical RWA disturbance model for incorporation into a performance assessment and enhancement framework developed by Gutierrez in reference [18]. In this framework, a disturbance model is used to drive a model of the spacecraft, or plant. Then performance outputs are compared against the requirements to assess the spacecraft/controller design. The development of the disturbance model is an important part of this process since the accuracy of the results obtained from the methodology depends heavily on the quality of the disturbance model. The performance assessment process is especially important for the next-generation telescopes, such as SIM and NGST, due to their stringent requirements. Since the RWA are expected to be the most significant source of jitter great care has been taken to develop an accurate RWA disturbance model. The model presented in this paper is based on the HST model, but is extended for application to any RWA through the development of a MATLAB toolbox that extracts the model parameters from steady state RWA vibration data. The empirical model can be represented in either the time or the frequency domain, and is most useful when used in combination with other RWA disturbance models, such as the stochastic model or the multiple wheel models described above.

2. EMPIRICAL MODEL

The Hubble Space Telescope (HST) requires high pointing accuracy and mechanical stability for the acquisition of science data. Therefore, characterization of RWA vibrations was important in the early stages of spacecraft design to allow prediction of performance degradation due to the operation of the wheels. To accomplish this goal, the HST RWA flight units were subject to a series of induced vibration tests. The results of these tests indicated that RWA disturbances are tonal in nature; i.e., the disturbance frequencies are a linear function of wheel speed [14]. Based on the data and the physics of a rotating imbalanced mass, the RWA disturbances are modelled as a series of discrete harmonics at frequencies that vary linearly with wheel speed and with amplitudes proportional to the wheel speed squared:

$$m(t) = \sum_{i=1}^n C_i \Omega^2 \sin(2\pi h_i \Omega t + \alpha_i), \quad (1)$$

where $m(t)$ is the disturbance force or torque, n is the number of harmonics included in the model, C_i is the amplitude coefficient of the i th harmonic, Ω is the wheel speed, h_i is the i th harmonic number and α_i is a random phase (assumed to be uniform over $[0, 2\pi]$) [17]. The harmonic numbers are non-dimensional frequency ratios that describe the relationship between the i th disturbance frequency, $\bar{\omega}_i$ and the spin rate of the wheel, Ω :

$$h_i = \frac{\bar{\omega}_i}{\Omega}. \quad (2)$$

Note that this model (equation (1)) yields disturbance forces and torques as a function of the wheel speed. It is a steady state model only; transient effects induced from changing wheel speeds are not considered.

The model parameters, h_i , C_i and n , are wheel dependent. As discussed previously, the two sources of RWA disturbances are flywheel imbalance and bearing imperfections. RWAs made by different manufacturers will not have the same designs and specifications. As a result, each wheel induces a unique set of disturbances. For example, a large wheel, that can provide high reaction torque, may produce larger amplitude disturbances than an RWA with a smaller flywheel. Also, flywheel imbalance and bearing imperfections are clearly not part of the RWA design. These anomalies occur during the manufacturing process and are difficult to control during operation. Therefore, each RWA has its own characteristic set of harmonic numbers and amplitude coefficients. As a result, in order to properly model a given wheel, it is necessary to perform vibration tests on the unit. Then, the model parameters can be determined empirically from the test data. To facilitate the parameter extraction process, a MATLAB toolbox that analyzes steady state RWA disturbance data and determines the harmonic numbers and amplitude coefficients for a model of the form described by equation (1) has been developed. The following sections present the formulation of such an empirical RWA model by first describing the algorithms used in the MATLAB functions and then illustrating the parameter extraction tools and validating the model using micro-vibration data from an ITHACO Space Systems E-type wheel.

3. RWA VIBRATION TESTING-ITHACO E WHEEL

An ITHACO Space Systems E-type wheel, model TW-50E300, was tested at the NASA Goddard Space Flight Center (GSFC). The wheel was integrated into a stiff cylindrical test fixture and hard-mounted to a Kistler force/torque table. The orientation of the wheel during the test was such that F_x and F_y are the radial forces, T_x and T_y are the radial torques, and F_z and T_z are the axial forces and torques respectively (see Figure 1). The wheel was started at 0 r.p.m. and full torque voltage was applied to the motor until the wheel saturated around 2400 r.p.m. The data were sampled at 3840 Hz for 390 s and eight channels of data corresponding to 12 load cell axes were obtained. The orientations of the load cell axes are shown in Figure 1. These channels were combined to derive the disturbance forces and torques at the mounting interface between the wheel and the table (frame **XYZ** in Figure 1). Note that although the vibration test was not conducted at steady state speeds, the time history can be subdivided into quasi-steady state time slices [19]. The continuous spin-up data were therefore transformed into 120 separate time histories and the average wheel speed for each slice was calculated.

The frequency content of the wheel disturbances can be best visualized by transforming the time histories to power spectral densities (PSDs) and creating a three-dimensional plot

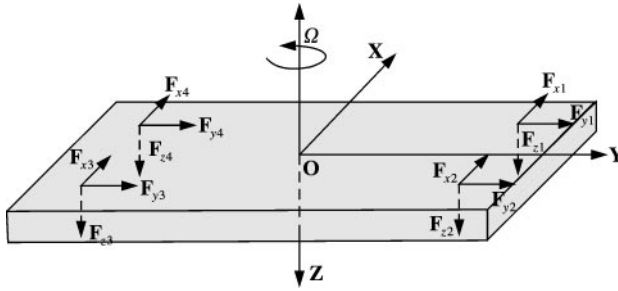


Figure 1. Schematic of Kistler force/torque table setup. Data from the four 3-axis load cells are combined to calculate the force/torque disturbances at the wheel interface in the **OXYZ** frame.

known as waterfall plot. An example of such a plot is shown in Figure 2(a). The average wheel speeds of the time histories are plotted along the x -axis. The frequency of the signals and the magnitude of the PSDs are shown along the y - and z -axis respectively. Taking a slice of the y - z plane of a waterfall plot results in the PSD of the RWA disturbances at a single wheel speed. Plotting the data in this form allows the identification of disturbance trends across both frequency and wheel speed. The waterfall plots of the six disturbance PSDs from the ITHACO Space Systems E-type wheel are shown in Figure 2. Note that diagonal ridges of disturbances in the x - y plane are visible in the data. The frequencies of these disturbances are linearly dependent on the wheel speed; as the speed of the wheel increases the disturbances slide along the frequency axis. These disturbances are the wheel harmonics. The fundamental harmonic is the largest of these disturbance ridges and is clearly visible in the radial forces and torques and the axial force. The smaller diagonal ridges are the super-harmonics caused by bearing imperfections and other disturbance sources within the RWA.

In addition to the diagonal ridges there are regions of disturbance amplification visible between 200 and 250 Hz in the first five waterfall plots. These disturbance amplifications form ridges in the x - y plane which are parallel to the y -axis; they are independent of the wheel speed. The frequency content suggests that these disturbances are due to structural modes in the wheel and/or test stand apparatus. However, given the geometry and design of the test fixture, its lowest mode is estimated to be greater than 300 Hz. Therefore, it can be concluded that disturbance amplifications below this frequency are due to structural modes of the RWA. A discussion of this component of the RWA disturbance environment is beyond the scope of this paper and will be addressed in a future publication.

The two radial force plots, Figures 2(a) and 2(b), show that the number and shape of the harmonics visible in these disturbances are similar. The same observation can be made with regard to the radial torques, Figures 2(c) and 2(d). This similarity is expected because the wheel is axisymmetric and therefore the radial forces/torques should differ only by 90° of phase. Therefore, the PSDs look nearly identical since no phase information is retained when the time histories are transformed to the frequency domain. The axial disturbance torque is not considered since the z -axis is the spin axis of the wheel, and the disturbance torque about this axis is negligible compared to the commanded torque.

4. EMPIRICAL DISTURBANCE MODELLING METHODOLOGY

The RWA Data Analysis and Disturbance Modelling (DADM) toolbox creates steady state disturbance models of the form shown in equation (1) from steady state reaction wheel

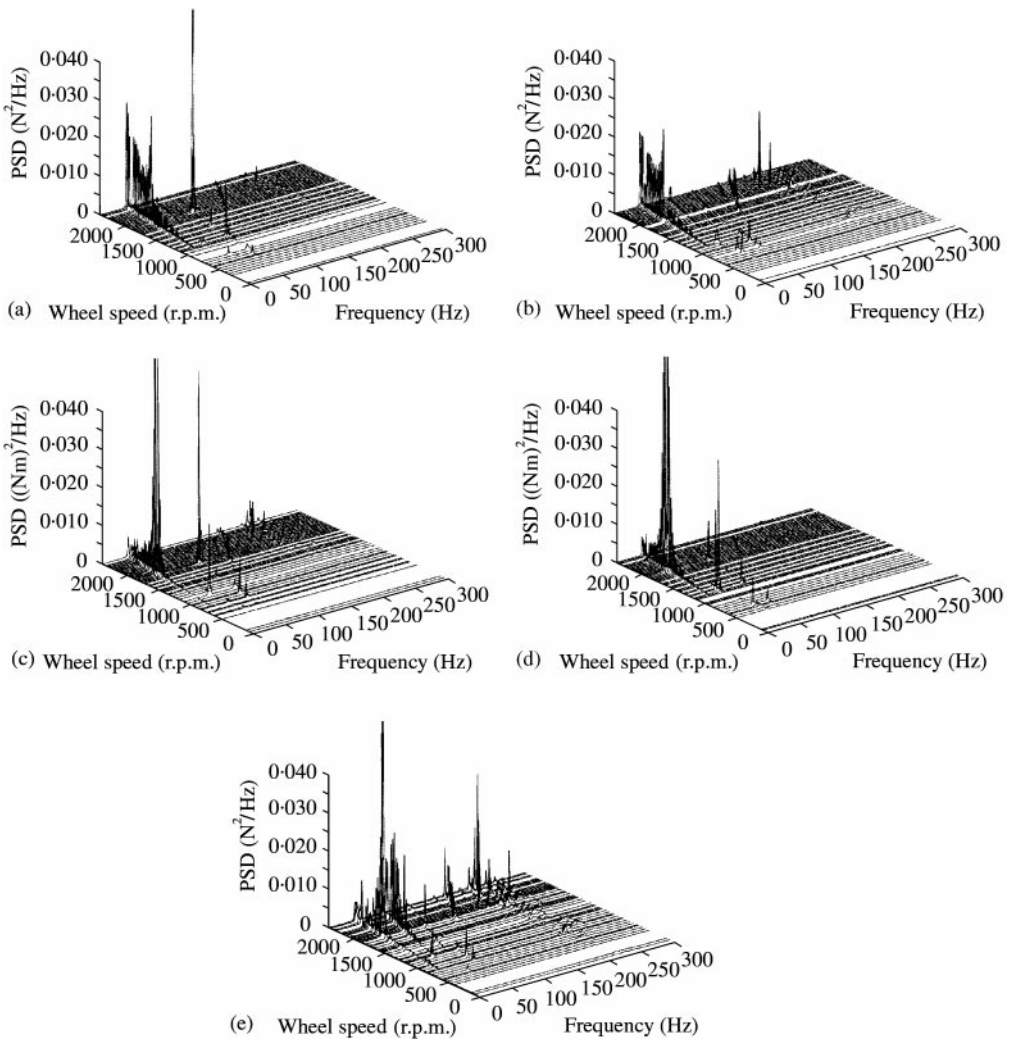


Figure 2. RWA disturbance data—IITHACO E-type wheel: (a) radial force, x direction; (b) radial force, y direction; (c) radial torque, x direction; (d) radial torque, y direction; (e) axial force, z direction.

disturbance data. The analysis tools extract the model parameters, h_i and C_i , from frequency domain data and generate plots for model validation. In this section, the data analysis and disturbance modelling process is discussed in detail using the development of a radial force disturbance model from the IITHACO Space Systems E-type wheel F_x and F_y data as an example.

4.1. OVERVIEW

Typical test results from one wheel include data for five disturbances: three forces (F_x , F_y , F_z) and two torques (T_x , T_y). Assuming the z -axis is the spin axis of the wheel, the F_x and F_y data are both radial force disturbances and are used in combination to create the radial force disturbance model. The use of both data sets should result in better correlation

between the model and the data since the number of data points in the sample space is doubled. Similarly, T_x and T_y are both radial torque data, and are used to create the radial torque model. The axial force disturbance model is created from the F_z , or axial force, data.

The RWA DADM process requires that experimental data from a given wheel be processed and stored in five data sets, one for each of the relevant disturbances, that include both the PSDs, \mathbf{S} , and amplitude spectra, \mathbf{A} , of the measured disturbances, the wheel speeds at which the data were taken, Ω , a frequency vector corresponding to the frequency domain data, \mathbf{f} , and the upper frequency limit of good data, f_{Lim} . Both \mathbf{S} and \mathbf{A} are row vectors of frequency domain data arranged such that the j th column corresponds to the PSD (or amplitude spectra) of the disturbance taken at the j th wheel speed, i.e., $\mathbf{S} = [S_1 \dots S_m]$. The upper frequency limit is determined by the frequency at which the data were sampled or the frequency of the first test stand mode. It is only desirable to use data that are not corrupted by test fixture dynamics. Therefore, if a test stand mode exists below the Nyquist frequency, f_{Lim} should be set at a frequency significantly lower than the test stand resonance. Otherwise, f_{Lim} is simply the Nyquist frequency.

The methodologies used to create the three disturbance models, radial force, radial torque and axial force, are quite similar. Therefore, only an overview of the radial forces will be given. Figure 3 summarizes the modelling procedure and should be referred to throughout the following discussion. In the initial stages of the analysis process, the F_x and F_y data sets are run through the algorithms separately, and a first generation of harmonic numbers, $(\mathbf{h}_{F_x})_1$ and $(\mathbf{h}_{F_y})_1$, are obtained from each data set. These quantities are then used to calculate the corresponding first generation of amplitude coefficients, $(\mathbf{C}_{F_x})_1$ and $(\mathbf{C}_{F_y})_1$. These parameters yield a model that can be compared with the experimental data. If the model comparison shows that there are extraneous harmonics in the model that are not validated by the data or that harmonics that are clearly visible in the data are not present in the model then the list of harmonic numbers is refined and the parameter extraction process is repeated. Additional iterations are performed on either data set (or both) until the harmonic numbers, \mathbf{h}_{F_x} and \mathbf{h}_{F_y} , match the experimental data to the user's satisfaction.

At this point in the analysis process the harmonic numbers, \mathbf{h}_{F_x} and \mathbf{h}_{F_y} , are combined to create a set of radial harmonic numbers, \mathbf{h}_{rad} . If a number is found in both lists (or if two numbers are close to each other) their average is included in \mathbf{h}_{rad} . Otherwise, \mathbf{h}_{rad} is simply the union of \mathbf{h}_{F_x} and \mathbf{h}_{F_y} . Once \mathbf{h}_{rad} has been determined it is used along with both the F_x and F_y data sets to calculate the amplitude coefficients for the radial disturbance model, \mathbf{C}_{rad} .

The amplitude coefficients are then validated with curve fit plots. If disturbance amplifications resulting from interactions between the structural wheel modes and harmonics are visible in the curve fits, the coefficients are run through an algorithm that removes these resonant effects. Finally, one more model/data comparison is performed as a final check. The radial model parameters should fit both the F_x and F_y data sets well. The radial force disturbance modelling procedure is described in detail in the following sections using the ITHACO Space Systems E-type wheel F_x data set as an example. The inputs and tolerances used to create this particular wheel model are listed in Table 1.

4.2. IDENTIFYING HARMONIC NUMBERS

The first step in the empirical modelling process is the extraction of the harmonic numbers, h_i , from the experimental data. An algorithm that individually examines all the amplitude spectra in a data set and locates peaks that are due to the wheel harmonics has been developed and implemented in MATLAB. Figure 4 presents a graphical

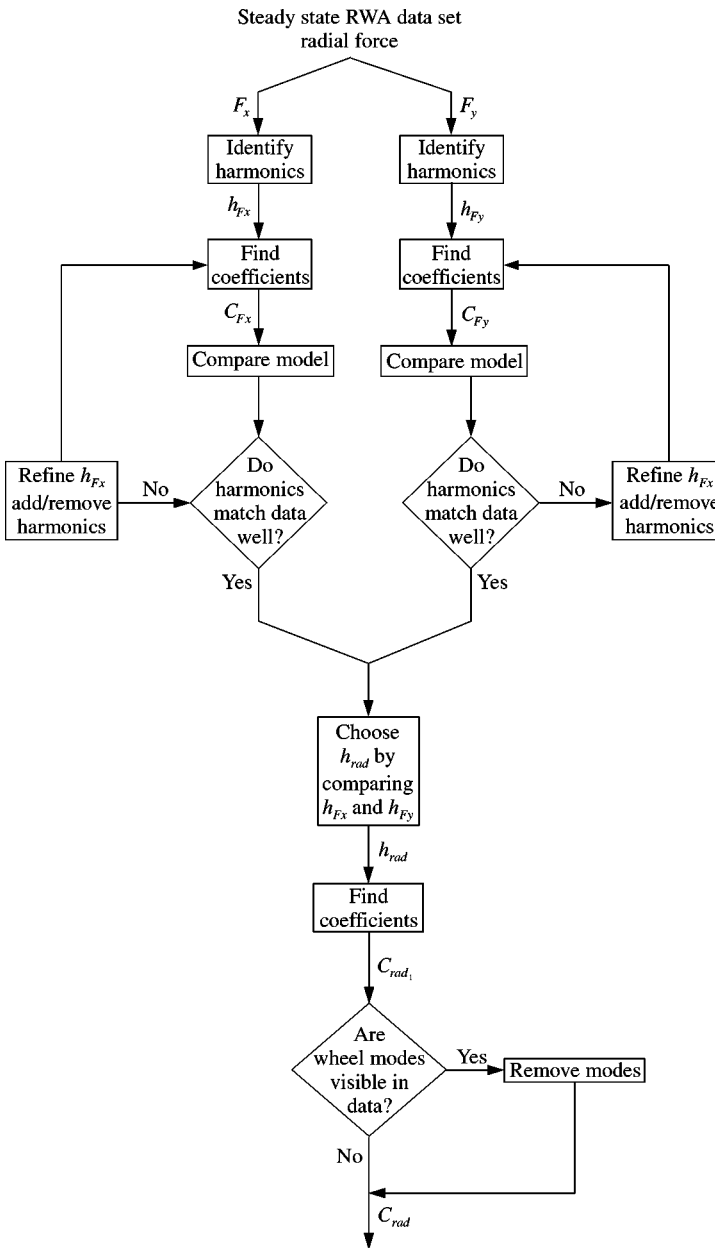


Figure 3. RWA data analysis process for radial force disturbance.

representation of the harmonic number identification algorithm and is referred to throughout the following discussion.

First, the frequencies, \mathbf{f} , are normalized by dividing the elements of the frequency vector by each of the speeds (in revolutions per second, r.p.s.) in the wheel speed vector, Ω . The result is m vectors of non-dimensional frequency ratios (where m is the total number of wheel speeds), \mathbf{f}_j^* , each corresponding to one wheel speed, Ω_j . Figure 5 demonstrates the normalization using the ITHACO Space Systems E-type wheel F_x data at $\Omega = 2000$

TABLE 1

Inputs for ITHACO E-type wheel radial force modelling

Name	Description	Size/value
m	No. of wheel speeds	120
n_f	No. of frequency points	640
\mathbf{f}	Frequency vector	640×1
f_{Lim}	Upper frequency limit	300 (Hz)
Ω_{F_x}	F_x data wheel speeds	1×120
Ω_{F_y}	F_y data wheel speeds	1×120
\mathbf{A}_{F_x}	F_x amplitude spectra	640×120
\mathbf{A}_{F_y}	F_y amplitude spectra	640×120
\mathbf{S}_{F_x}	F_x PSDs	640×120
\mathbf{S}_{F_y}	F_y PSDs	640×120
N_σ	Noise isolation tolerance	2
ε	Binning tolerance	0.02
P_0	Bin percentage threshold	25%

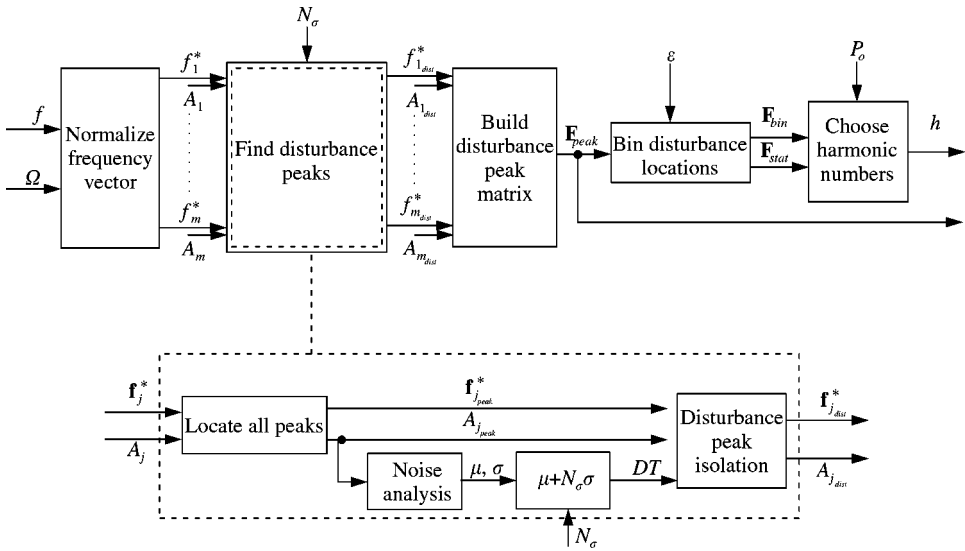


Figure 4. Harmonic number identification algorithm with detail of *find disturbance peaks* block.

revolutions per minute, r.p.m. (or 33.33 r.p.s.). In the upper plot, the amplitude spectrum, A , is plotted versus frequency. In the lower plot the same data are plotted as a function of the normalized frequency, \mathbf{f}^* . Note that the largest peak in the amplitude spectra occurs at $f^* = 1.0$. This peak is caused by the fundamental harmonic disturbance ($h_i = 1$).

The next step in the algorithm is to identify the normalized frequencies of the disturbance peaks in the amplitude spectra as indicated by the block labelled *find disturbance peaks* in Figure 4. The figure contains an exploded view of the block showing the disturbance peak identification process for one set of amplitude spectra and normalized frequencies. Note that within the main algorithm this process is executed m times. First, all the peaks in the amplitude spectra are identified by differencing A_j and locating sign changes in the

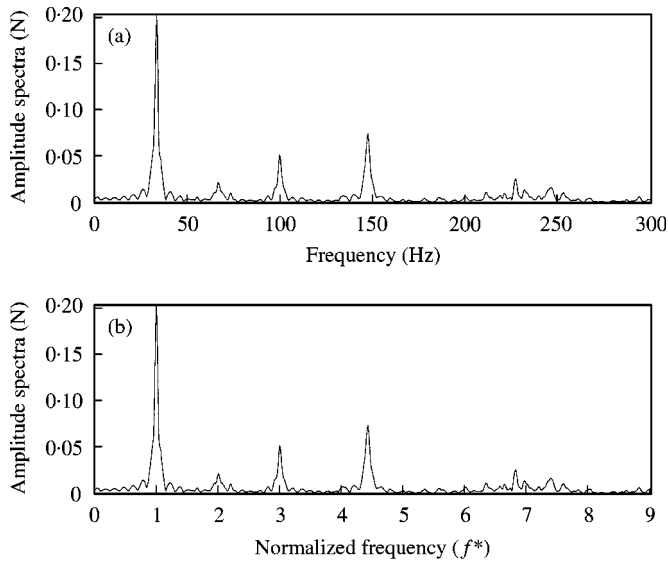


Figure 5. Frequency normalization of ITHACO E-type wheel F_x data (2000 r.p.m.): (a) amplitude spectrum versus frequency; (b) amplitude spectrum versus normalized frequency.

differenced data. The quantities $f_{j_{peak}}^*$ and $A_{j_{peak}}$ are the normalized peak frequencies and amplitudes respectively. For example, each peak identified in ITHACO Space Systems E-type wheel amplitude spectra A at $\Omega = 2000$ r.p.m. is shown in Figure 6(a) marked with an “x”. Note that *all* of the peaks in the data are marked. It is highly unlikely that all of these peaks are a result of harmonic disturbances. Some may be due to noise or may be a result of taking the FFT of the time history data. Therefore, a method was developed to discriminate between disturbance peaks and noise peaks.

Noise is isolated from the disturbance harmonics in the block labelled *noise analysis*. The MATLAB histogram function is used to bin the elements of $A_{j_{peak}}$ according to amplitude. Assuming that the noise peaks are all of roughly the same amplitude and account for the largest bin in the histogram allows a disturbance amplitude threshold, DT , to be determined. All spike amplitudes that fall in or below the largest histogram bin are considered noise. The remaining spikes are considered possible harmonic disturbances. See Figure 6(b) for an example. The disturbance amplitude threshold is then defined as

$$DT = \mu_{noise} + N_{\sigma} \sigma_{noise}, \quad (3)$$

where μ_{noise} and σ_{noise} are the mean and standard deviation of the spike amplitudes identified by the histogram. The parameter N_{σ} is a user-defined tolerance level. Its default value is 3, but can be adjusted according to the signal-to-noise ratio of the data. The ITHACO Space Systems E-type wheel data, for example, were sampled at a relatively high frequency (3840 Hz) and for a long time. Therefore, a small frequency resolution and good signal-to-noise ratio were obtained, which allows the use of a lower noise isolation tolerance, $N_{\sigma} = 2$.

All peaks with an amplitude below the disturbance amplitude threshold are not included in the final vector of disturbance peaks. This part of the algorithm is represented in the diagram by the block labelled *disturbance peak isolation*. The final outputs of the *find disturbance peaks* algorithm are a vector of normalized disturbance peak frequencies,

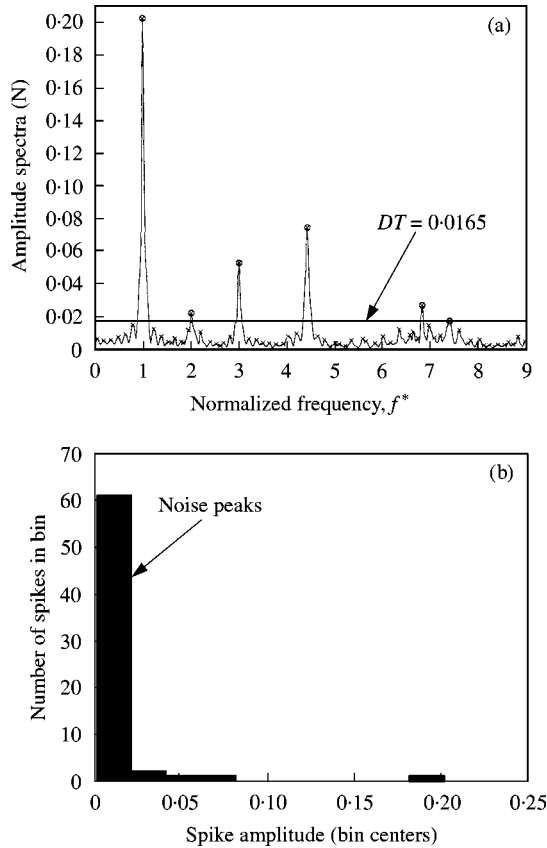


Figure 6. Disturbance peak identification in ITHACO E-type wheel F_x data (2000 r.p.m.): (a) peak identification with $N_\sigma = 3$: *, all peaks (1st iteration); O, disturbance peaks (2nd iteration); (b) noise isolation histogram, $\mu = 0.0059$, $\delta = 0.0035$.

$\mathbf{f}_{J_{dist}}^*$ and a vector of disturbance peak amplitudes, $\mathbf{A}_{J_{dist}}$. The results of running the ITHACO Space Systems E-type wheel data through the function are shown in Figure 6(a). The disturbance threshold is indicated by the horizontal line, and the dark circles indicate the disturbance peaks. Note that the majority of the smaller noise peaks lie below the disturbance threshold. Once the disturbance peaks are identified in all m sets of amplitude spectra and normalized frequency vectors a matrix of normalized peak frequencies, \mathbf{F}_{peak} , with each column corresponding to a different wheel speed, is built. This matrix is used to identify the harmonic numbers.

A true harmonic disturbance should occur at the same normalized frequency over all wheel speeds. Therefore, a binning algorithm is used to search \mathbf{F}_{peak} for matching frequencies across wheel speeds. Initially, the first column of the matrix is used as the baseline case, \mathbf{f}_{base}^* . The first entry in the baseline column is denoted the “test entry”, f_0^* , and placed into a bin. All of the other columns are then searched for normalized frequencies, f^* , that are within $\pm \epsilon$ of the test entry (where ϵ is a user-defined tolerance):

$$f_0^* - \epsilon \leq f^* \leq f_0^* + \epsilon. \tag{4}$$

All f^* satisfying equation (4) are placed into the bin with f_0^* and their locations in \mathbf{F}_{peak} are set to zero. If two or more normalized frequencies in the same column satisfy equation (4)

their average is placed in the bin, and both entries are set to zero. Averaging ensures that a possible harmonic will only be accounted for once at each wheel speed. When the entire matrix has been searched, the second element of \mathbf{f}_{base}^* becomes the test entry and a new bin is created. The process continues until all elements of \mathbf{f}_{base}^* have been considered. At this point, the second column becomes \mathbf{f}_{base}^* and the search is repeated. The algorithm continues in this manner until all non-zero elements of \mathbf{F}_{peak} are binned. The results of the binning algorithm are a matrix of the binned normalized frequencies, \mathbf{F}_{bin} (with the k th column corresponding to the k th bin) and a second matrix containing the statistics for each bin, \mathbf{F}_{stat} . The first row of \mathbf{F}_{stat} is the average, or center, of the bins, $\bar{f}_{bin_k}^*$, and the second row contains the number of elements in the bins, N_{bin_k} .

In the final block of Figure 4 the harmonic numbers are chosen from \mathbf{F}_{stat} . A metric, P_k , is defined as the percentage of possible wheel speeds in which a given normalized peak frequency was found:

$$P_k = \frac{N_{bin_k}}{N_{poss_k}} 100\%, \quad (5)$$

where N_{poss_k} is the total possible number of elements in the k th bin. In general, N_{poss_k} should be equal to the number of wheel speeds in the data set. However, this assumption does not always hold due to the frequency range of the data set. The value of f_{Lim} may limit the number of wheel speeds in which a given normalized peak frequency is visible. For example, as mentioned earlier, the E Wheel is free of corruption by test stand dynamics in the range [0, 300] Hz. Any data above 300 Hz is not used in the modelling process. The normalized frequency 1.0 corresponds to 8.3 Hz when the wheel is spinning at 500 r.p.m. and to 56.7 Hz at 3400 r.p.m. Since both frequencies lie within the frequency range [0, 300] a disturbance at $f^* = 1.0$ can be observed at all wheel speeds. The normalized frequency 5.98, on the other hand, corresponds to 49.8 Hz at 500 r.p.m. and 339 Hz at 3400 r.p.m. In this case, f^* lies within the specified frequency range for only a subset of the wheel speeds. The value of N_{poss_k} is therefore not the same over all k bins.

The metric P_k can be considered a measure of the strength of a disturbance across wheel speeds, and is used to identify wheel harmonics from the list of bin centers, $\bar{f}_{bin_k}^*$ in \mathbf{F}_{stat} . If P_k is greater than a user-defined threshold, P_0 , then $\bar{f}_{bin_k}^*$ is defined to be a harmonic number and placed into a new vector, \mathbf{h} . The outputs of the harmonic number identification algorithm are this vector of harmonic numbers, \mathbf{h} , and the matrix of normalized disturbance peak frequencies, \mathbf{F}_{peak} . Both outputs are necessary for the next step of the modelling process.

To create a complete wheel model, the harmonic number identification process described above is performed on the three force and two torque disturbances. Then, the radial force and radial torque model harmonic numbers, \mathbf{h}_{rad} and \mathbf{h}_{tor} , are determined by comparing and combining the harmonic numbers extracted from the F_x and F_y data and the T_x and T_y data respectively. The axial force harmonic numbers, \mathbf{h}_{axi} , are the harmonic numbers extracted from the F_z data.

4.3. CALCULATING AMPLITUDE COEFFICIENTS

The next step in the empirical modelling process is the extraction of the amplitude coefficients, C_i , from the experimental data. Figure 7 presents a graphical representation of the algorithm used to calculate the amplitude coefficients given a steady state RWA data set, the harmonic numbers, \mathbf{h} , and matrix of normalized disturbance peak frequencies, \mathbf{F}_{peak} .

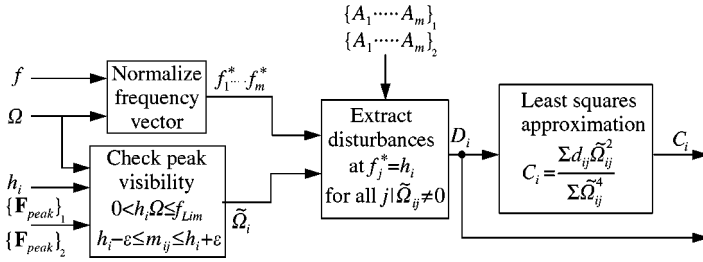


Figure 7. Amplitude coefficient calculation algorithm.

The block diagram details the process for one harmonic and its corresponding amplitude coefficient. In practice, the algorithm is repeated for each harmonic in the model.

Least-squares approximation methods are used to calculate the amplitude coefficients for the HST RWA disturbance model [14]. The magnitude of the disturbance force (or torque) is assumed to be related to the wheel speed as

$$\tilde{d}_{ij} = K_i \Omega_j^2, \tag{6}$$

where \tilde{d}_{ij} is the expected disturbance force (or torque) at the frequency corresponding to the i th harmonic at the j th wheel speed and K_i is a constant. The error between the actual disturbance and the expected disturbance at the i th harmonic and the j th wheel speed, e_{ij} is then

$$e_{ij} = d_{ij} - K_i \Omega_j^2, \tag{7}$$

where d_{ij} is the experimentally measured disturbance force at the i th harmonic and j th wheel speed. The amplitude coefficient, C_i , is defined as the value of K_i that minimizes this error. An expression for C_i is obtained by squaring equation (7), summing over the wheel speeds and solving for the K_i that minimizes the squared error, e_{ij}^2 :

$$C_i = \frac{\sum_{j=1}^m d_{ij} \Omega_j^2}{\sum_{j=1}^m \Omega_j^4}. \tag{8}$$

Recall that during the initial stages of the radial force/torque modelling procedure the coefficients are calculated from a single data set, but the final model coefficients are calculated using two data sets (see Figure 3). The RWA DADM algorithm uses equation (8) to compute the coefficients for either the single or double data set case as shown in Figure 7. In the following discussion, multiple data set extraction of radial force amplitude coefficients from the ITHACO Space Systems E-type wheel F_x and F_y data will be used as an example.

The first block in Figure 7 represents the normalization of the frequency vector, \mathbf{f} . The resulting non-dimensional frequency vectors, $\{\mathbf{f}_1^* \dots \mathbf{f}_m^*\}$ are used along with \mathbf{A} , \mathbf{F}_{peak} , Ω and \mathbf{h} to determine the disturbance forces, d_{ij} , at each harmonic number over all wheel speeds. It is important to note that a disturbance at the i th harmonic may not be visible in all of the amplitude spectra in the data set. A disturbance peak can be undetectable for one of two reasons. If the frequency corresponding to h_i for a given wheel speed, Ω_j , is not within the frequency range of good data, $[0, f_{Lim}]$, the disturbance amplitude at this frequency may be

corrupted and is not included in the calculation of the amplitude coefficient. In addition, not all disturbances that fall within the frequency range are visible at all wheel speeds. For example, disturbances are often more difficult to identify in data taken at low wheel speeds due to a low signal-to-noise ratio. Therefore, the data must meet certain peak detection conditions to be included in the calculation of C_i .

Recall that both the matrix of amplitude spectra, \mathbf{A} , and \mathbf{F}_{peak} contain m columns, each corresponding to one wheel speed. Defining the quantity \mathcal{D}_j which contains the amplitude spectra, wheel speed, normalized frequency vector, normalized peak locations, and upper frequency limit of good data associated with one wheel speed, $\mathcal{D}_j(A_j, \mathbf{f}_j^*, \mathbf{F}_{peak}, \Omega_j, f_{Lim})$ allows the peak detection conditions to be written as

$$\mathcal{D}_j = \{0 < h_i \Omega_j \leq f_{Lim}\} \cap \{f^* \in \mathbf{F}_{peak_j} | h_i - \varepsilon \leq f^* \leq h_i + \varepsilon\}. \quad (9)$$

The first condition in equation (9) ensures that the frequency corresponding to the harmonic for Ω_j is within the frequency range of good data. The second condition uses the matrix of detected normalized peak frequencies, \mathbf{F}_{peak} , obtained from the harmonic number identification algorithm to ensure that a disturbance peak at $f^* = h_i$ is detectable in the amplitude spectra.

The extraction of disturbance amplitudes for use in the amplitude coefficient calculation is done one wheel speed at a time. The amplitude spectrum provides an estimation of the signal amplitude over frequency. Therefore, if \mathcal{D}_j satisfies both of the above conditions the magnitude of the disturbance force/torque at the frequency corresponding to the i th harmonic is simply the value of A_j at the normalized frequency $f^* = h_i$. The disturbance magnitude is assigned to d_{ij} , and the wheel speed is assigned to $\tilde{\Omega}_{ij}$. However, if one or both of the conditions are not satisfied, the data for that wheel speed is not included in the calculation and both d_{ij} and $\tilde{\Omega}_{ij}$ are set to zero. This process is continued for all wheel speeds, until two vectors of length m , one of disturbance amplitudes, \mathbf{D}_i , and one of corresponding wheel speeds, $\tilde{\Omega}_i$, are created. In general, $\tilde{\Omega}_i$ would be equal to the input vector Ω , but since all of the wheel speeds may not be included in the amplitude coefficient calculation for a given harmonic due to lack of disturbance peak visibility, each C_i is computed using a distinct subset of wheel speeds, $\tilde{\Omega}_i$. The vectors \mathbf{D}_i and $\tilde{\Omega}_i$ are manipulated and summed as shown in equation (8) to obtain C_i .

Curve-fit plots are useful for both removing harmonics from the model and assessing the quality of the fit between the data and the disturbance force predicted by C_i . The plots for the 1.0 and 4.42 harmonics of the ITHACO Space Systems E-type wheel data (F_x and F_y) are shown in Figure 8. The circles represent the disturbance amplitudes of the experimental data over the different wheel speeds, \mathbf{D}_i . Note that some of the circles lie on the x -axis. These points are from wheel speeds which did not meet the conditions in equation (9). The solid line is the curve generated using the calculated C_i and equation (6).

Notice in the curve fit plot for $h_1 = 1.0$ that the data points are not distributed evenly across wheel speeds, but are clustered at high wheel speeds. Recall that when the vibration tests were conducted, full torque was applied to the wheel and it was allowed to spin up until it reached saturation around 2300 r.p.m. As a result, a large portion of the data was taken while the wheel was saturated at its maximum speed. Therefore, when the data were processed into quasi-steady state data sets, the highest wheel speed was represented multiple times in the wheel speed vector and frequency domain data matrices. The algorithm used to calculate the amplitude coefficients ensures that the uneven wheel speed distribution does not result in an unequal weighting of the data points when the amplitude coefficient is calculated. If a data point from a given wheel speed is included more than once in the vector \mathbf{D}_i , the wheel speed is also included an equal number of times in $\tilde{\Omega}_i$.

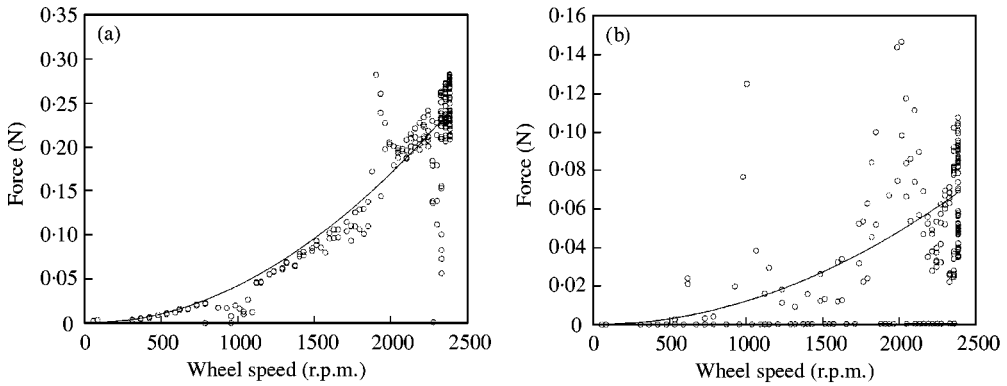


Figure 8. Amplitude coefficient curve fits for ITHACO E-type wheel radial force data: (a) $h_1 = 1.0$; (b) $h_5 = 4.42$; —, model; \circ , data.

If a curve fit is not based on enough data points there cannot be a high degree of confidence in the resulting amplitude coefficient, and the harmonics are removed from the model. The data from the high wheel speeds could not be included in the curve fit because the frequencies corresponding to this harmonic are not within the frequency range of good data. Therefore, it is often difficult to predict the amplitude coefficients for the higher harmonics.

In addition, the curve fits allow assessment of the validity of the assumption that the disturbance amplitudes are related to the wheel speed squared (equation (6)). In Figure 8(a), the data points lay right along the theoretical curve. This result suggests that the assumption of equation (6) holds for the fundamental harmonic. In contrast, the curve fit for $h_5 = 4.42$, Figure 8(b), is not quite as good. The curve follows the general trend of the data, but the points do not lie along the predicted line. The same is true for all harmonics except the fundamental. Equation (6) can be derived by considering the physics of a statically and dynamically imbalanced rotating mass. The fundamental harmonics is the result of exactly this situation whereas the other harmonics are due to bearing imperfections and other effects that are more difficult to model physically. Therefore, it makes sense that the wheel speed squared law does not necessarily hold for the sub- and super-harmonics.

Figure 8(b) also shows large disturbance amplifications in the form of resonant peaks at both 1000 and 2000 r.p.m. These amplifications occur when the frequency of the harmonic approaches the frequency of one of the structural wheel modes. The form of the empirical model does not present a convenient method to account for these modal excitations. Therefore, the empirical model will be used to model only the wheel harmonics. As a result, the modal interactions seen in the figure should not be included in the calculation of the amplitude coefficient. The structural modes and the disturbance amplifications are incorporated into a second RWA model which is the subject of a future publication.

An algorithm was developed that isolates the effects of the structural mode from the harmonic disturbances and is shown in a block-diagram representation in Figure 9. The outputs from the original amplitude coefficients calculation are denoted \bar{C}_i and \bar{D}_i to differentiate between coefficients calculated with and without modal effects. These quantities are input to the algorithm along with Ω , the harmonic index, i , and the wheel speed range affected by the structural mode, $[\Omega_l, \Omega_u]$. For example, consider the third harmonic of the ITHACO Space Systems E-type wheel radial torque model ($h_7 = 5.57$) shown in Figure 10. The lighter circles and dashed curve are the initial results of the amplitude coefficient calculation.

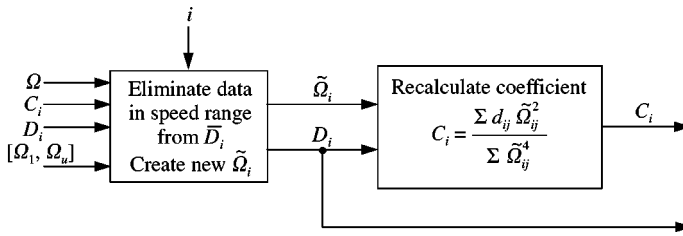


Figure 9. Structural mode isolation algorithm.

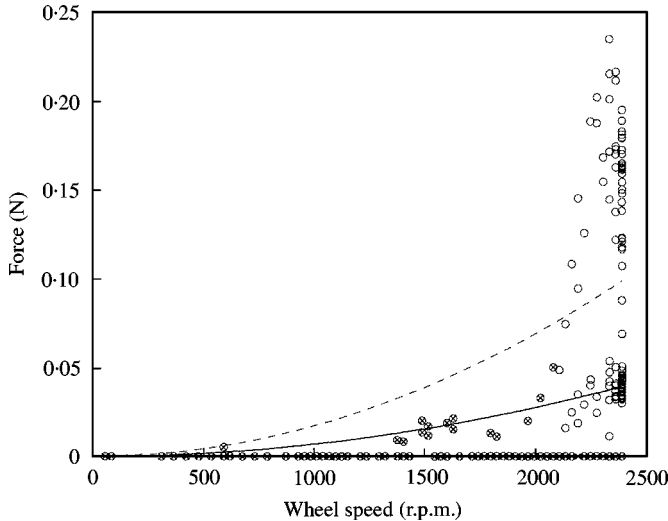


Figure 10. Effects of internal wheel modes on amplitude coefficient curve fit; $h_7 = 5.57$ (ITHACO E-type wheel radial force): \circ , with modal effects, $C_7 = 1.73 \times 10^{-8}$; \times , w/o modal effects, $C_7 = 0.69 \times 10^{-8}$.

Note that there is a large increase in force amplitude in the data around 2300 r.p.m. The resonant effect of the structural mode is removed from the amplitude coefficient calculation by removing the data points associated with speeds in the affected range from $\bar{\mathbf{D}}_i$. Then, a new disturbance magnitude vector, \mathbf{D}_i , and corresponding wheel speed vector, $\tilde{\Omega}_i$ are created and used to calculate the corrected amplitude coefficient, C_i .

The resulting curve fit without the modal effects included is also shown in Figure 10. The dark x's and the solid curve correspond to \mathbf{D}_7 and C_7 and do not include the resonance points, while the lighter circles and dashed curve correspond to the original coefficient calculation based on all points, $\bar{\mathbf{D}}_7$ and \bar{C}_7 . Note that including data with the resonance behavior causes an over-estimation of the disturbance force over all wheel speeds (dashed curve). When the resonant data are removed from the coefficient calculation (solid curve) the amplitude coefficient is decreased by 60% and there is a much better fit between the theoretical curve and the data between 1500 and 2000 r.p.m.

Seven harmonics have been identified for the ITHACO Space Systems E-type wheel radial force disturbance model with the analysis toolbox. A harmonic at $h_i = 5.00$ and those greater than 5.57 are eliminated from the model due to low-confidence amplitude coefficient curve fits. In most of these cases, the only significant peaks are a result of disturbance

TABLE 2

Disturbance amplification in radial force harmonics

h_i	Wheel speed range (r.p.m.)	Amplification source	$\bar{C}_i \times 10^7$ (N/r.p.m. ²)	$C_i \times 10^7$ (N/r.p.m. ²)
1-0	1900-2000	Radial rocking (negative whirl)	0.4200	0.4155
	800-1300	Radial rocking (negative whirl)		
2-0	2200+	Unknown	0.0846	0.0832
3-0	1800-2000	Radial rocking (positive whirl)	0.0734	0.0543
	1150-1400	Radial rocking (positive whirl)		
4-0	2100+	Unknown	0.0629	0.0621
	900-1100	Radial rocking (positive whirl)		
4-42	1800-2150	Unknown	0.1188	0.1100
5-37	2200+	Radial translation	0.0780	0.0524
5-57	2200+	Radial translation	0.1729	0.0690

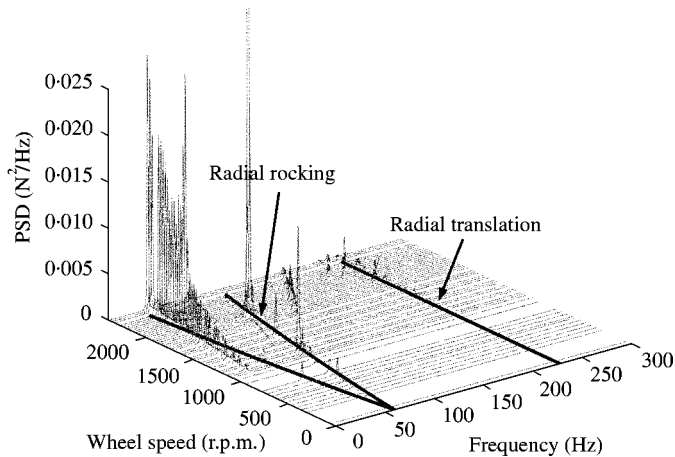


Figure 11. Waterfall comparison of radial force model and ITHACO E-type wheel F_x data showing modal excitation.

amplification by structural modes. Once the affected points are removed from the calculation there are not enough data left to accurately predict the amplitude coefficient. The fact that these harmonics can not be observed at low wheel speeds indicates that the disturbances at these frequencies are most likely small relative to the identified harmonics. Therefore, their omission from the model should not have a large effect on the degree of correlation between the model and the data.

Table 2 lists the affected speed ranges, probable amplification sources and amplitude coefficients (with and without amplification) for each of the affected harmonics in the ITHACO Space Systems E-type wheel data. The amplification source was determined by examining the waterfall plot comparison of the radial force data and model, Figure 11. In this plot, the frequencies of the radial structural wheel modes are labelled and highlighted with solid dark lines. The frequencies of these modes are based on information reported by

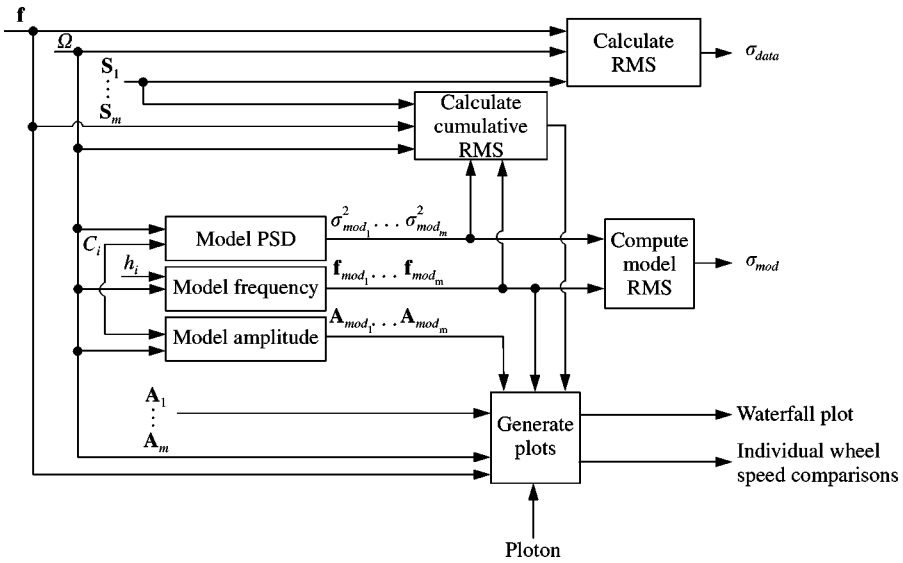


Figure 12. Model comparison and validation algorithm.

ITHACO Space Systems [15]. The coefficient curve fit plot for the fundamental harmonic shows a disturbance amplification around 2000 r.p.m. This amplification is also visible in the waterfall plot at the same wheel speed. Note that the amplification occurs at the point where the harmonic crosses the negative whirl of the rocking mode. This observation suggests that the disturbance amplification is due to the excitation of the radial rocking mode by the first harmonic. The sources of the other amplifications are determined in this manner and are listed in Table 2. In some cases the amplification source is listed as “unknown”. These harmonics show disturbance amplifications at high wheel speeds and frequencies that do not correspond to either of the radial modes. The source of disturbance amplification is unclear in these cases.

4.4. MODEL VALIDATION: COMPARING TO DATA

Model validation is achieved through comparison of the empirical model to the experimental data. A block diagram representation of the comparison algorithm is shown in Figure 12. The inputs include the vectors of model parameters, \mathbf{h} and \mathbf{C} , and the data set components, \mathbf{S} , \mathbf{A} , \mathbf{f} , Ω and f_{Lim} . The outputs are a series of plots and vectors of length m containing the RMS of the model, σ_{mod} , and the data, σ_{data} , at each of the wheel speeds.

The empirical model is created using the harmonic numbers, amplitude coefficients and Ω . Recall from equation (1) that the forces and torques are modelled as discrete harmonic disturbances at frequencies dependent upon h_i and with amplitudes proportional to the wheel speed squared. The disturbance frequencies for a given wheel speed, $\bar{\omega}_j$, are determined by

$$\bar{\omega}_j = \mathbf{h}\Omega_j. \tag{10}$$

The vector $\bar{\omega}_j$ is a vector of discrete disturbance frequencies for the j th wheel speed and is the same length as \mathbf{h} . Similarly, vectors of disturbance amplitudes, $\mathbf{A}_{mod,j}$ corresponding to

$\bar{\omega}_j$ are created based on the assumption that the disturbance amplitude from the i th harmonic at the j th wheel speed is

$$A_{mod_{ij}} = C_i \Omega_j^2. \tag{11}$$

The matrices \mathbf{A}_{mod} and $\bar{\omega}$, which are analogous to the experimental quantities \mathbf{A} and \mathbf{f} , are used to generate model/data comparison plots.

In addition, the PSD of the model, S_{mod_j} , is calculated for comparison to the experimental data. An expression for the model PSD as a function of frequency and wheel speed is derived from the definition of the autocorrelation, $R_X(\tau)$:

$$R_X(\tau) = R_X(t, t + \tau) = E[X(t)X(t + \tau)]. \tag{12}$$

Substituting $m(t)$ (equation (1)) for $\mathbf{X}(t)$ in equation (12) and assuming that α_i is a random variable uniformly distributed between 0 and 2π and that α_i and α_j are statistically independent, the expression for the autocorrelation of the empirical model becomes

$$R_m(\tau) = \sum_{i=1}^n \frac{C_i^2 \Omega_j^4}{2} \cos(\Omega_j h_i \tau). \tag{13}$$

The mean square of a random process is equal to its autocorrelation evaluated at $\tau = 0$. Therefore, assuming that $m(t)$ is both stationary and zero mean, the variance of the empirical model is

$$\sigma_{mod_j}^2 = R_m(0) = \sum_{i=1}^n \frac{C_i^2 \Omega_j^4}{2}. \tag{14}$$

Equations (13) and (14) are then used to derive the spectral density function of the empirical model. The autocorrelation function of a single harmonic process and its corresponding spectral density are given in reference [20] as

$$R_x(\tau) = \sigma_x^2 \cos(\omega_0 \tau), \tag{15}$$

$$S_x(\omega) = \sigma_x^2 \left[\frac{1}{2} \delta(\omega + \omega_0) + \frac{1}{2} \delta(\omega - \omega_0) \right]. \tag{16}$$

Substituting equation (14) into equation (12) and setting $h_i \Omega_j = \omega_0$ results in an autocorrelation of the same form as that in equation (15). Therefore, the PSD of the empirical model is of the same form as that in equation (16). After making the necessary substitutions the one-sided PSD of the empirical model, $S_{mod_j}(\omega)$, is

$$S_{mod_j}(\omega) = \sum_{i=1}^n \frac{C_i^2 \Omega_j^4}{2} \delta(\omega - \bar{\omega}_j). \tag{17}$$

Note that the empirical model PSD consists of a series of discrete impulses occurring at frequencies, $\bar{\omega}_j$, with amplitudes equal to the variances of the harmonics, $\sigma_{mod_{ij}}^2$. The vectors $[\sigma_{mod_1}^2, \dots, \sigma_{mod_m}^2]$, which are outputs of the “model PSD” block in Figure 12, consist of the PSD amplitudes for the discrete harmonics at all m wheel speeds. The matrix of these vectors, σ_{mod}^2 is analogous to \mathbf{S} and is used for model/data comparison.

The RMS values of the model and data are calculated for each wheel speed. The area under the PSD of a random process is equal to the mean square. Therefore, the data RMS for a given wheel speed, σ_{data_j} , is simply the square root of the area under the PSD, S_j .

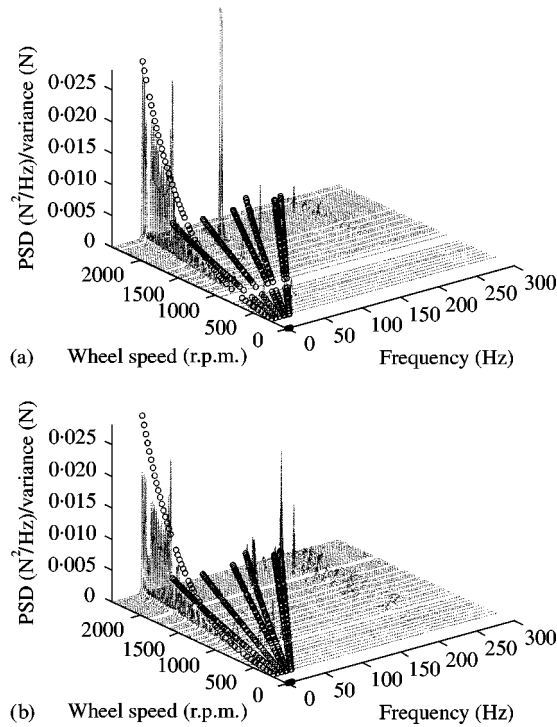


Figure 13. Waterfall comparison of radial force model and ITHACO E-type wheel data. (a) F_x data; (b) F_y data; —, data; ○, model.

A MATLAB function is used to perform the integration across frequency and obtain this value for each wheel speed. The RMS of the model is calculated using the assumption that the random process $m(t)$ is stationary and zero mean. The RMS of a zero mean process is simply the square root of its variance:

$$\sigma_{mod_j} = \sqrt{\sum_{i=1}^n \frac{C_i^2 \Omega_j^4}{2}}. \quad (18)$$

The vectors of RMS values, σ_{mod} and σ_{data} are used to compare the model and the data to assess model validity.

Three types of plots are generated by the model validation function. The first is a waterfall plot that overlays the model PSDs and the data PSDs as shown in Figure 13. In this figure, the ITHACO Space Systems E-type wheel data PSDs are plotted as continuous lines and the radial force empirical model PSDs are represented with circles. It is important to note that the units of amplitude (z -axis) for the data and model are not equivalent. The data PSDs are continuous over frequency and have amplitudes with units of N^2/Hz , but the model PSDs consist of series of discrete impulses with amplitudes which have units of N^2 and are equal to the variance, or the area under the corresponding peak in the continuous PSD, of the harmonic disturbance. Therefore this type of plot should not be used to validate the amplitude coefficients of the model. Instead, the waterfall plot is useful for validating the harmonic numbers.

Note that both the F_x and F_y waterfall plots show good correlation between the disturbance frequencies of the data and the model indicating that the harmonic numbers are

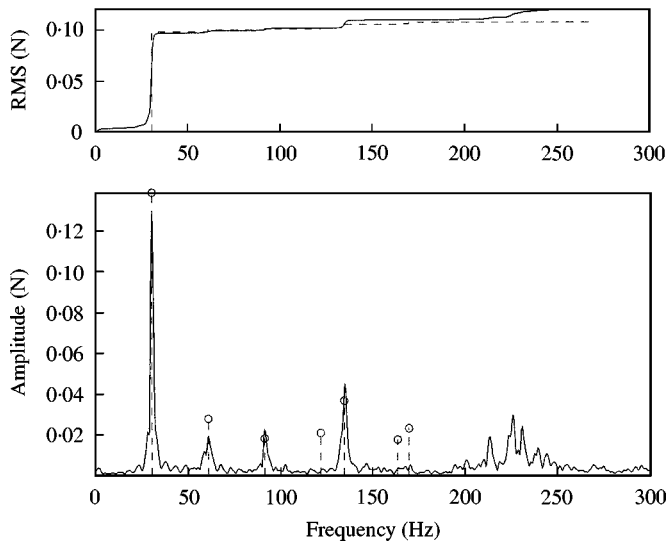


Figure 14. PSD comparison of radial force model to F_x data (ITHACO E-type wheel) with cumulative r.m.s. at 1800 r.p.m.: —, data, r.m.s. = 0.12; ---/○, model, r.m.s. = 0.107.

captured accurately. The diagonal lines of circles lie on top of the diagonal ridges seen in the data. During the first iterations of the modelling process such plots are extremely useful for finding harmonics which may have been missed or erroneously identified. It does appear that there may be some higher harmonics that are not included in the model (due to large uncertainty in the amplitude coefficients), but the most significant disturbances are captured.

The second type of plot generated is shown in Figure 14. The lower plot compares the amplitude spectra of the data and model for one wheel speed (1800 r.p.m. in this example). The continuous curve is the data amplitude spectrum, and the discrete impulses, marked with circles, are the radial force model amplitudes. In this form, both data and model amplitudes have the same units and can be compared directly, allowing validation of the amplitude coefficients. Note that the amplitude of the first harmonic, which is the fundamental, matches the amplitude of the data quite well. The comparison of the higher harmonics, on the other hand, is not as good. This discrepancy is most likely due to the assumption that the disturbance force is proportional to the wheel speed squared (equation (6)). As mentioned earlier, this assumption is valid for the fundamental harmonic but begins to break down with the higher harmonics.

The cumulative r.m.s. curves, which represent the r.m.s. as a function of frequency, for both the model and the data, are plotted above the amplitude spectra. These curves offer a second method of validating the amplitude coefficients. Ideally, the model r.m.s. will be close to the data r.m.s. and the contributions to the r.m.s. from the harmonics will be comparable. In this example, the first harmonic is the largest contributor to the r.m.s. in both the data and the model and its amplitude is captured in the model quite accurately. However, the overall model r.m.s. under-predicts the data r.m.s. by 11%. The cumulative r.m.s. curve indicates that the discrepancy is due to high-frequency energy in the data that is not captured in the model. The missing energy can most likely be attributed to harmonics that are not included in the model due to low-confidence amplitude coefficient curve fits. These results indicate that overall, the empirical model captures the harmonic RWA disturbances reasonably well at this particular wheel speed.

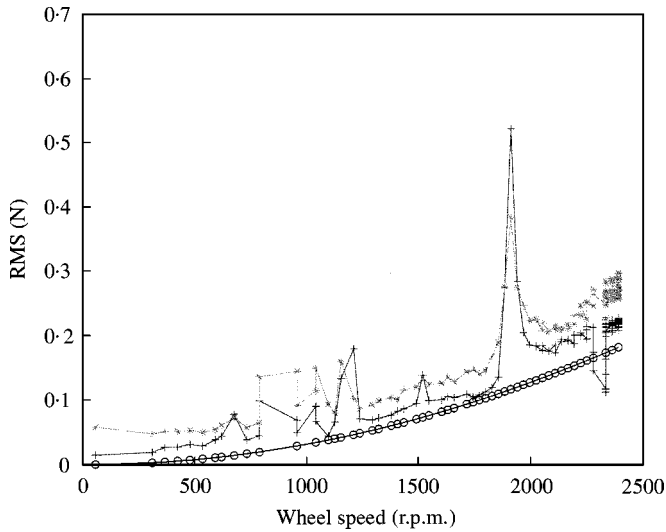


Figure 15. r.m.s. comparison of empirical model and ITHACO E-type wheel data: radial forces: +, F_x data; *, F_y data; O, radial model.

The third type of model/data comparison used for model validation is shown in Figure 15. In this plot, the r.m.s. values of the data and the model are plotted as a function of wheel speed. In effect, the plot is simply an integration of the waterfall plot across frequency. The solid curves, marked with “+” and “*” are the r.m.s. values for the F_x and F_y data, respectively, and are quite similar, as is expected. The figure shows that over most wheel speeds the model under-predicts the data slightly, but not by a significant amount. However, there is a large amount of energy in the data between 1800 and 2000 r.p.m. that is not captured in the model. Referring to Table 2, note that both the first and third harmonics excite the structural rocking mode of the wheel in this speed range. Therefore, a discrepancy between the data and the model in this range exists because the empirical model does not account for the structural modes of the wheel. The smaller peaks in the data r.m.s. between 800 and 1200 r.p.m. can also be attributed to the structural wheel modes by similar reasoning.

5. CONCLUSIONS

A set of MATLAB functions has been created to extend the HST model and facilitate the empirical modelling process. The toolbox extracts empirical model parameters from steady state RWA vibration data allowing the creation of an empirical disturbance model for any given RWA assuming that the wheel disturbances are a series of harmonics at discrete frequencies with amplitudes proportional to the wheel speed squared. The toolbox takes advantage of data analysis techniques to allow the user to quickly create disturbance models for a number of RWA. These models can be used in a disturbance analysis framework to conduct trade studies on different types of RWA, enabling the engineer to select the wheel that is best suited for a given application.

Steady state vibration data from an ITHACO Space Systems E-type wheel were used as an example to illustrate the capability of the toolbox and to validate the model. Waterfall

plots and r.m.s. comparison plots were used to compare the model to the data allowing an assessment of the accuracy of the empirical model and the performance of the toolbox. The data correlation for the ITHACO Space Systems E-type wheel model is quite good over most wheel speeds. The waterfall plot comparison indicates that the disturbance frequencies are identified accurately; the harmonic numbers in the model are also visible in the data. The amplitudes of the disturbances also seem reasonable since the r.m.s. values of the data and model are close over the wheel speed ranges that do not include disturbance amplifications. For example, at 1800 r.p.m. the model r.m.s. is 0.107 and the data r.m.s. is 0.12, an error of only 11%. Over all wheel speeds between 56 and 2400 r.p.m. the model under-predicts the data by an average error of 20%; the model disturbance amplitudes are within a factor of two of the data.

The under-prediction of the ITHACO Space Systems E-type wheel model is most pronounced over discrete ranges of speeds that show significant disturbance amplifications in the data that are not matched by the model. These peaks in r.m.s. result when the structural wheel modes are excited by the harmonic disturbances. Such a peak is visible in the E Wheel r.m.s. plot at about 1900 r.p.m. The data r.m.s. at this wheel speed is 0.52 N and the model r.m.s. is only 0.117 N. At this wheel speed the model under-predicts the data by 77%. Such large discrepancies exist in the affected wheel speed ranges because the internal wheel flexibility is not captured in the empirical model. The overall r.m.s. error of 20% is driven by these disturbance amplifications.

It is concluded that although the empirical model captures the wheel harmonics and identifies the disturbance frequencies well, it alone is not an accurate RWA disturbance model. Excitation of the structural wheel modes by the harmonics can cause large disturbance amplifications that must be included in the model to accurately predict the effects of the disturbances on the spacecraft during operation. An analytical disturbance model has been developed to take the resonant effects into account and is the subject of a future publication. It is a combination of the analytical and empirical models that does the best job of capturing the RWA disturbance environment. Therefore, the empirical model and parameter extraction methodology is a major component of an accurate RWA disturbance model.

The MATLAB toolbox described in this paper can be applied to steady state micro-vibration data from any reaction wheel to provide the harmonic numbers and amplitude coefficients that are necessary components of the complete disturbance model for a given RWA. In this way, the toolbox generalizes the empirical modelling process for application to any mission in which structural dynamics and control play a key role in meeting performance requirements.

ACKNOWLEDGMENTS

The ITHACO E-type wheel data discussed in this paper were obtained thanks to Gary Mosier (Goddard Space Flight Center), Gary Brown (Goddard Space Flight Center) and Mr. Oliver DeWeck (MIT Space Systems Laboratory). Dr. Homero Gutierrez also contributed through his previous work, technical suggestions and support.

The work described in this paper was conducted in part at the Massachusetts Institute of Technology under a contract with the Jet Propulsion Laboratory, California Institute of Technology and in part at the Jet Propulsion Laboratory, California Institute of Technology, under a contract with the National Aeronautics and Space Administration. Additional support for the work was provided by TRW Space & Electronics Group through a graduate student fellowship.

REFERENCES

1. R. S. DANNER and S. UNWIN (editors) 1999 *Space Interferometry Mission: Taking the Measure of the Universe*. Pasadena: Jet Propulsion Laboratory, California Institute of Technology.
2. R. A. LASKIN 1995 in *American Institute of Aeronautics and Astronautics Aerospace Sciences Meeting and Exhibit, AIAA 95-0825*. Technology for space optical interferometry.
3. R. A. LASKIN and M. SAN MARTIN 1989 in *Proceedings of AAS/AIAA Astrodynamics Specialist Conference, AAS 89-424*, 369–395. Control/structure system design of a spaceborne optical interferometer.
4. O. DE WECK, D. MILLER and H. GUTIERREZ 1998 in *Proceedings of the 34th Liege International Astrophysics Colloquium*, 269–273. Noordwijk, Netherlands: European Space Agency. Structural dynamics and controls for NGST—a preliminary study.
5. B. BIALKE 1998 in *Proceedings of the 21st Annual AAS Rocky Mountain Guidance and Control Conference, AAS paper 98-0634*, 483–496. San Diego: Univelt, Inc. High fidelity mathematical modeling of reaction wheel performance.
6. T. MARSHALL, T. GUNDERMAN and F. MOBLEY 1991 in *Proceedings of the Annual Rocky Mountain Guidance and Control Conference, AAS paper 91-038*, 119–138. San Diego: Univelt, Inc. Reaction wheel control of the MSX satellite.
7. L. P. DAVIS, J. F. WILSON, R. E. JEWELL and J. J. RODEN 1986. Hubble space telescope reaction wheel assembly vibration isolation system.
8. T. FUKUDA, H. HOSOKAI and N. YAJIMA 1986 *Bulletin of the JSME* **29**, 3121–3125. Flexibility control of solar battery arrays (3rd Report, vibration and attitude control with consideration of the dynamics of a reaction wheel as an actuator).
9. S. SABNIS, F. SCHMITT and L. SMITH 1976 *Sperry Flight Systems, Jet Propulsion Laboratory NASA Technical Report N76-27336*. Magnetic bearing reaction wheel.
10. J. A. BOSGRA and J. J. M. PRINS 1982 in *Automatic Control in Space (9th Symposium)*, 449–458. Testing and investigation of reaction wheels.
11. L. P. DAVIS, D. CUNNINGHAM and J. HARRELL 1994 in *AIAA/ASME/ASCE/AHS/ASC Structures, Structural Dynamics, and Materials Conference, AIAA paper 94-1651*, 2655–2665. Advanced 1.5 Hz passive viscous isolation system.
12. Sperry Flight Systems 1976 *NASA/Marshall Space Flight Center, NASA Technical Report N76-18213*. An evaluation of reaction wheel emitted vibrations for large space telescope.
13. K. J. PENDERGAST and C. J. CHAUWECKER 1998 in *SPIE Conference on Space Telescopes and Instruments*, Vol. 3356 (Part 2 of 2), 1078–1094. Use of a passive reaction wheel jitter isolation system to meet the advanced X-ray astrophysics facility imaging performance requirements.
14. M. D. HASHA 1986 *Space Telescope Program Engineering Memo SSS 218*. Reaction wheel mechanical noise variations.
15. B. BIALKE 1997 in *20th Annual American Aeronautical Society Guidance and Control Conference, AAS paper 97-038*. A compilation of reaction wheel induced spacecraft disturbances.
16. B. LI, G. GODDU and M. CHOW 1998 in *Proceedings of the American Control Conference*, 2032–2036. Detection of common motor bearing faults using frequency-domain vibration signals and a neural network based approach.
17. G. W. NEAT, J. W. MELODY and B. J. LURIE 1998 *IEEE Transactions on Control Systems Technology* **6**, 689–700. Vibration attenuation approach for spaceborne optical interferometers.
18. H. L. GUTIERREZ 1999 *Ph.D. Thesis, Massachusetts Institute of Technology*. Performance assessment and enhancement of precision controlled structures during conceptual design.
19. O. DE WECK 1999 *Master's Thesis, Massachusetts Institute of Technology*. Integrated modeling and dynamics simulation for the next generation space telescope.
20. P. H. WIRSCHING, T. L. PAEZ and H. OORTIZ 1995 *Random Vibrations: Theory and Practice*. New York: John Wiley & Sons Inc.